Impacts of the rudder profile on manoeuvring performance of ships

Liu, Jialun; Quadvlieg, Frans; Hekkenberg, Robert

DOI
10.1016/j.oceaneng.2016.07.064

Publication date
2016

Document Version
Accepted author manuscript

Published in
Ocean Engineering

Citation (APA)
Liu, J., Quadvlieg, F., & Hekkenberg, R. (2016). Impacts of the rudder profile on manoeuvring performance of ships. *Ocean Engineering*, *124*, 226-240. https://doi.org/10.1016/j.oceaneng.2016.07.064

Impacts of the rudder profile on manoeuvring performance of ships

Jialun Liu[a,*], Frans Quadvlieg[b], Robert Hekkenberg[a]

[a] *Delft University of Technology, Mekelweg 2, 2628 CD, Delft, The Netherlands.*
[b] *Maritime Research Institute Netherlands (MARIN), Haagsteeg 2, 6700 AA, Wageningen, The Netherlands.*

Abstract

The profile of a ship rudder influences the forces it generates, which in turn influence the manoeuvring performance of a ship. Thus, rudder forces and moments should be calculated considering the profile. Instead of an empirical estimation of the rudder normal force coefficient, this paper applies a RANS method to determine the hydrodynamic characteristics of various profiles, i.e. lift and drag coefficients. The RANS method is validated with a classic NACA 0012 profile and applied to 9 profiles from the NACA series, the wedge-tail series, and the IFS series. Furthermore, the 2D open-water RANS results are corrected for the effects of the propeller slipstream and the rudder aspect ratio. New regression formulas of the normal force coefficients are proposed for the tested profiles. These formulas are then integrated into a standard MMG model. Taking the KVLCC2 tanker as a reference ship, the manoeuvring model is validated with free-running tests executed by MARIN. Finally, the manoeuvring performance of the reference ship with various rudder profiles are quantified with turning and zigzag manoeuvres. The simulation results confirm that the wedge-tail series is most effective (largest manoeuvring forces) while the NACA series is most efficient (highest lift to drag ratio) among the tested profiles. The IFS series achieves a balance of effectiveness and efficiency.

Keywords: Rudder profiles, ship manoeuvrability, RANS methods, manoeuvring simulations, KVLCC2

Nomenclature

Abbreviations

CFD	Computational Fluid Dynamics
RANS	Reynolds-Averaged Navier-Stokes
IFS	Institute für Schiffbau
NACA	National Advisory Committee for Aeronautics

*Corresponding author.
Email address: J.Liu@tudelft.nl (Jialun Liu)

Re	Reynolds number	
SST	Shear Stress Transport	

Greek Symbols

α_R	Effective rudder angle	(rad)
β	Ship drift angle	(rad)
β_P	Drift angle at propeller position	(rad)
δ	Rudder angle	(rad)
$\dot{\delta}$	Rudder rate	($^\circ$ s^{-1})
η	Ratio of propeller diameter to rudder span	(−)
γ_R	Flow straightening coefficient of the rudder	(−)
ℓ	Flow-straitening factor due to the yaw rate	(−)
κ	Experimental constant for expressing u_R	(−)
Λ_G	Rudder geometric aspect ratio, $\Lambda_G = B_R/C_R$	(−)
∇	Ship displacement volume	(m^3)
ψ	Ship heading angle	(rad)
ρ	Water density	(kg m^{-3})

Roman Symbols

A_D	Advance of turning circle test	(m)
A'_D	Non-dimensional advance of turning circle test, $A'_D = A_D/L_{pp}$	(−)
a_H	Rudder force increase factor	(−)
A_R	Rudder lateral area without the horn part	(m^2)
T_D	Tactical diameter of turning circle test	(m)
T'_D	Non-dimensional tactical diameter of turning circle test, $T'_D = T_D/L_{pp}$	(−)

B_R	Rudder span	(m)
B_{wl}	Maximum moulded breadth at design water line	(m)
C_b	Block coefficient	(−)
C_N	Normal force coefficient of the rudder with specific aspect ratio in propeller slipstream	(−)
C_R	Rudder chord length	(m)
C_{N_∞}	Normal force coefficient of the rudder with infinite aspect ratio in open water	(−)
D_P	Propeller diameter	(m)
F_N	Rudder normal force	(N)
I_z	Yaw moment of inertia of the ship around centre of gravity	(kg m^2)
J_P	Propeller advance ratio	(−)
J_z	Added moment of inertia of the ship around centre of gravity	(kg m^2)
K_T	Propeller thrust coefficient	(−)
L_{pp}	Length between perpendiculars	(m)
m	Ship mass	(kg)
m_x	Added mass due to ship motion in x-direction	(kg)
m_y	Added mass due to ship motion in y-direction	(kg)
N_H	Hydrodynamic moment due to hull acting on the ship around z-axis	(N m)
n_P	Propeller revolution	(s^{-1})
N_R	Hydrodynamic moment due to rudder acting on the ship around z-axis	(N m)
$\dot{r}$	Yaw acceleration around midship z axis	(rad s)
r	Yaw rate around midship z axis	(rad s)
T	Ship draught	(m)
t	Rudder profile section thickness	(m)

T_P	Propeller thrust	(N)
t_P	Propeller thrust deduction factor in manoeuvring motions	(−)
t_R	Steering resistance deduction factor	(−)
$\dot{u}$	Ship acceleration in the direction of x axis	($\mathrm{m\,s^{-2}}$)
u	Surge speed in the direction of x axis, $u = V\cos\beta$	($\mathrm{m\,s^{-1}}$)
u_0	Service speed of the ship (the initial speed for manoeuvring simulations)	($\mathrm{m\,s^{-1}}$)
u_G	Longitudinal speed in the direction of x axis at centre of gravity, $u_G = u$	($\mathrm{m\,s^{-1}}$)
u_R	Longitudinal velocity of the inflow to rudder	($\mathrm{m\,s^{-1}}$)
$\dot{v}$	Ship acceleration in the direction of y axis	($\mathrm{m\,s^{-2}}$)
V	Ship velocity on midship, $V = \sqrt{u^2 + v^2}$	($\mathrm{m\,s^{-1}}$)
v	Sway speed in the direction of y axis on midship, $v = -V\sin\beta$	($\mathrm{m\,s^{-1}}$)
V_A	Propeller advance speed	($\mathrm{m\,s^{-1}}$)
v_G	Sway speed in the direction of y axis at centre of gravity, $v_G = v + x_G r$	($\mathrm{m\,s^{-1}}$)
V_R	Rudder inflow velocity	($\mathrm{m\,s^{-1}}$)
v_R	Lateral velocity of the inflow to rudder	($\mathrm{m\,s^{-1}}$)
w_P	Wake factor at propeller position in manoeuvring	(−)
w_R	Wake factor at rudder position in manoeuvring	(−)
w_{P_0}	Wake factor at propeller position in straight moving	(−)
x_G	Longitudinal position of centre of gravity in $o - xyz$	(m)
X_H	Hydrodynamic force due to hull acting on midship in x-direction	(N)
x_H	Longitudinal position of acting point of additional lateral force	(m)
X_P	Hydrodynamic force due to propeller acting on midship in y-direction	(N)
x_P	Longitudinal position of propeller in $o - xyz$	(m)

X_R	Hydrodynamic force due to rudder acting on midship in x-direction	(N)
x_R	Longitudinal position of rudder in $o - xyz$	(m)
y_+	Non-dimensional first cell height	(−)
Y_H	Hydrodynamic force due to hull acting on midship in x-direction	(N)
Y_R	Hydrodynamic force due to rudder acting on midship in y-direction	(N)

1. Introduction

Rudders are the most common steering devices of ships. They determine the response of a ship to navigation orders and affect the manoeuvrability. To satisfy the mandatory manoeuvrability criteria of the International Maritime Organization (IMO) (International Maritime Organization, 2002b,a), a ship must achieve sufficient turning forces and moments from its rudders. Furthermore, the rudder induced resistance also impacts the overall fuel consumption. Thus, rudders do not only affect navigation safety but transport efficiency as well. In the initial design stage of a rudder, a decision has to be made regarding the profile, which has significant impacts on its hydrodynamic performance for manoeuvring (Kim et al., 2012). Additionally, Liu and Hekkenberg (2016) reviewed the design choices of rudders and their impacts on rudder performance in ship manoeuvrability, fuel consumption, and rudder cavitation.

Yasukawa and Yoshimura (2014) introduced the standard MMG model for ship manoeuvring simulations. The MMG model calculates rudder forces (X_R and Y_R) and moments (N_R) based on the rudder's normal force (F_N) as the following:

$$F_N = 0.5\rho A_R V_R^2 C_N, \tag{1}$$

where ρ is the water density, A_R is the rudder lateral area, V_R is the rudder inflow velocity, and C_N is the rudder normal force coefficient, which depends on the rudder profile. Routinely, C_N is obtained by empirical formulas (Fujii, 1960; Fujii and Tsuda, 1961, 1962) as the following:

$$C_N = 6.13 \sin \alpha_R \frac{\Lambda_G}{\Lambda_G + 2.25}, \tag{2}$$

where Λ_G is the rudder geometric aspect ratio, which is the ratio of the rudder span (B_R) to the rudder chord length (C_R), α_R is the effective rudder angle. Normally, the rudder effectiveness is judged by the rudder side force (Y_R), which primarily depends on A_R, V_R, and C_N as shown by Eq. 1 and Eq. 2.

The rudder area (A_R) is determined by the rudder span and chord, which are constrained by design draught and capacity of the steering gear. Achieving the required rudder area may not be a problem for seagoing ships, but it

is critical for inland vessels (Liu et al., 2015). When the rudder size is limited, a twin-rudder or multiple-rudder configuration is the solution. This solution, for example, is frequently applied to inland vessels with multiple rudders and very large seagoing ships with twin rudders.

The rudder inflow velocity (V_R) relates to the ship speed, the propeller working load, the propeller rate of revolution, and the location of the rudder relative to the propeller. However, these parameters are rarely optimised on purpose for the rudder effectiveness. Therefore, the rudder normal force coefficient (C_N) mainly depends on the rudder profile. As the empirical method (Eq. 2) only considers the aspect ratio, it does not enable an analysis of the profile impact on rudder forces and moments regarding the ship manoeuvring performance.

To obtain the normal force coefficients of various profiles, the rudder hydrodynamic characteristics should be analysed, i.e. the lift and drag coefficients. These coefficients are traditionally obtained in wind tunnels (Thieme, 1965), towing tanks (Vantorre, 2001), or by Computational Fluid Dynamics (CFD) (Söding, 1998; El Moctar, 2001). Even though CFD methods may encounter challenges in convergence and accuracy, they are convenient to study various cases as a primary study. Thus, this paper applies a Reynolds-Averaged Navier-Stokes (RANS) method to achieve the actual rudder force coefficients of different profiles for manoeuvring simulations.

This paper presents manoeuvring simulations of a KVLCC2 tanker based on RANS calculation results of 9 rudder profiles from 3 series, i.e. National Advisory Committee for Aeronautics (NACA), Institute für Schiffbau (IFS), and wedge-tail. Section 2 discusses the characteristics of the rudder profiles. Section 3 describes the mesh and solver of the applied RANS method, which is then validated with wind tunnel results of a NACA 0012 profile. Section 4 presents the hydrodynamic characteristics of the tested profiles. These results are then corrected with the propeller slipstream and the rudder aspect ratio impacts. Section 5 introduces the mathematical model used for manoeuvring simulations, which is validated with free-running tests of the KVLCC2 tanker with a NACA 0018 profile. Section 6 presents the manoeuvring performance of the KVLCC2 tanker with various rudder profiles in turning and zigzag manoeuvres. Section 7 obtains conclusions.

2. Rudder profiles

Profiles are generally classified into different families differing in the maximum thickness and its location. Various rudder families have different hydrodynamic characteristics (Thieme, 1965). The choice of profiles should depend on the ship particulars and sailing conditions. Molland and Turnock (2007) presented an overview of rudder types. This paper compares the hydrodynamic characteristics of 9 profiles from 3 common families, i.e. NACA, wedge-tail, and IFS.

2.1. NACA

To achieve an efficient rudder, which can generate sufficient lift with minimum drag, the NACA series is most widely used (Kim et al., 2012). The conventional NACA 00 series is suitable for a large range of ships while the low-drag NACA 65/66 series is more applicable for high-speed vessels which are vulnerable to cavitation (Molland and Turnock, 2007). In this paper, 5 NACA profiles are used for validation and comparison as shown in Fig. 1. The NACA 0012 profile is taken as the validation profile for the RANS method. The NACA 0018 profile is applied for the validation of the manoeuvring model as it is the original rudder profile for the KVLCC2 tanker. Furthermore, NACA 0015, NACA 0020, and NACA 0025 profiles are tested to compare with other series of similar thickness.

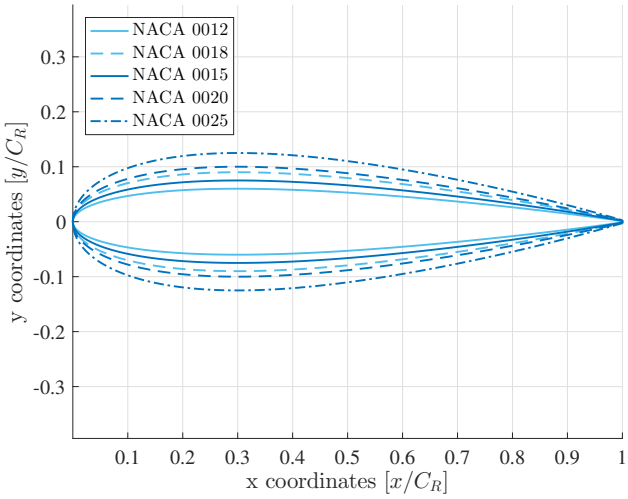

Figure 1: Tested NACA profiles.

2.2. Wedge-tail

Inland vessels commonly use wedge-tail and fishtail (Schilling) profiles to improve the rudder effectiveness at slow speed in shallow water. A basic approach to generate a wedge-tail rudder is to attach a tail to a NACA profile. Commonly, fishtail rudders have smoother geometry and better performance than wedge-tail rudders. However, little information is publicly available regarding the fishtail geometries. wedge-tail and fishtail rudders commonly have larger stall angles than the NACA series as the tails can generate high lift but with extra drag (Thieme, 1965; Molland and Turnock, 2007). As no uniform geometry was found in the literature, we designed three wedge-tail rudders based on the NACA 0015, NACA 0020, and NACA 0025 geometries. These wedge-tail profiles have a concave point at 0.95 C_R and a trailing edge thickness of 0.1 C_R as demonstrated in Fig. 2.

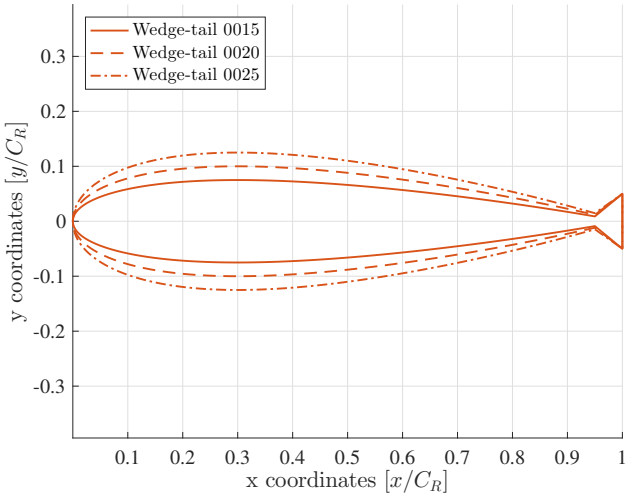

Figure 2: Tested wedge-tail profiles.

2.3. IFS

The IFS series is developed to achieve a steeper slope of the lift coefficient, a delay stall, and an increase of the maximum lift coefficient by optimising the pressure distribution around the profile (Molland and Turnock, 2007). Thieme (1965) presented wind tunnel tests of the IFS series. Fig. 3 shows the 3 tested IFS profiles, i.e. IFS56 TR15, IFS61 TR25, and IFS62 TR25.

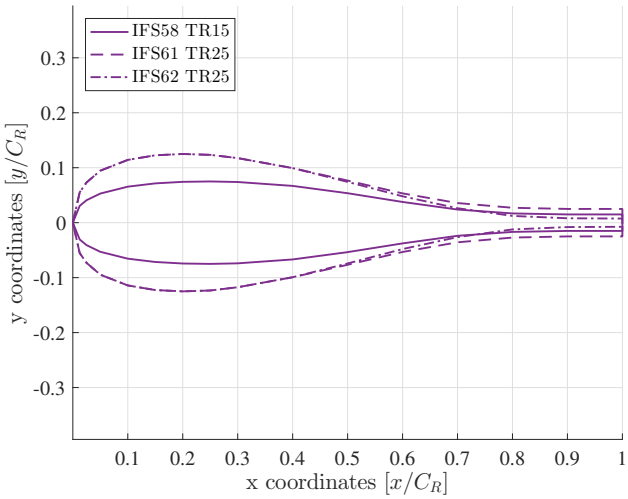

Figure 3: Tested IFS profiles.

3. RANS methods

To obtain the hydrodynamic characteristics of each profile, this paper applies a RANS method. This section introduces the mesh generation, the solver selection, and the validation of the model based on a NACA 0012 profile.

3.1. Mesh generation

A mesh presents the physical model in a discrete form on which the governing equations can be resolved numerically. To obtain reliable CFD solutions, the mesh has to be sufficiently refined in the area where high gradients of fluid characteristics exist. This paper applies hybrid meshes, which have structured inflation layers around the profile and unstructured cells filling the domain. Hybrid meshes are easier to generate and converge for complex geometries than structured meshes. In addition, hybrid meshes can better simulate the viscous effects than pure unstructured meshes. Fig. 4 illustrates the mesh for a NACA 0012 profile. Meshes for other tested profiles are generated with the same strategy.

The fluid material is incompressible water. The boundary conditions for left, top and bottom, and right sides of the domain are set as velocity-inlet, symmetry (no-shear wall), and pressure-outlet as shown in Fig. 4. The test Reynolds number is 6×10^6. Above this value, small impacts of the Re on the lift and drag coefficients are found (Ladson, 1988). The corresponding inflow speed is $6.0289\,\mathrm{m\,s^{-1}}$ for a rudder model with 1 m chord length. The inflow is kept normal to the inlet boundary while the profile is rotated by the specified angle of attack. The mesh is implemented in a rectangular domain of 60 C_R in width and 90 C_R in length to minimise the influence of the far-field boundaries. The profile locates in the front of the domain, with 30 C_R to left, top, bottom and 59 C_R to right respectively. This domain is sufficiently large to minimise the influence of the boundary locations on the rudder hydrodynamics while not excessively large resulting in a waste of computation resource and time. To improve the accuracy of the solution and capture the wake area, an inner domain is defined to refine the mesh around the rudder. The dimension of the inner domain is illustrated in Fig. 4. For the wall effect, the profile is covered by 50 structured inflation layers. The rest of the domain is filled with unstructured meshes.

3.2. Numerical methods

Instead of resolving the continuous governing partial equations, the Navier-Stokes equations are actually solved in the discrete form with a numerical solver. This paper applies a Pressure-Based Coupled-Solver (PBCS) in ANSYS Fluent 16.1. The PBCS solves momentum and pressure-based continuity equations in a coupled manner and speeds up the overall convergence (Keating, 2011). A second-order upwind spatial scheme is used to decrease the discretisation errors. Three common turbulence models are Spalart-Allmaras, Realisable $k-\epsilon$, and $k-\omega$ shear stress transport ($k-\omega$ SST) to construct the turbulent effects. Eleni et al. (2012) evaluated the performance of these three models concluding that the $k-\omega$ SST model has a good agreement with the experimental data. Because it combines the best of the $k-\omega$

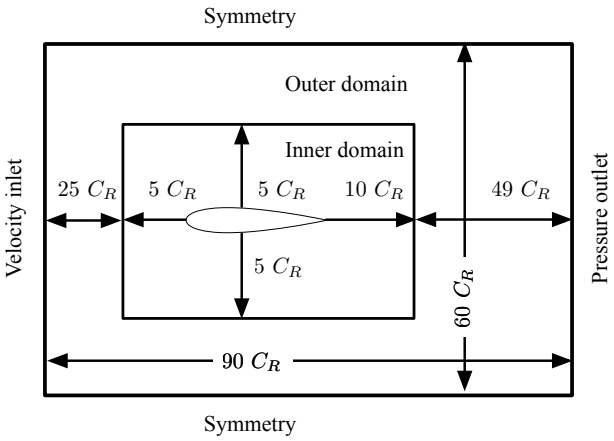

(a) Test domain and boundary conditions.

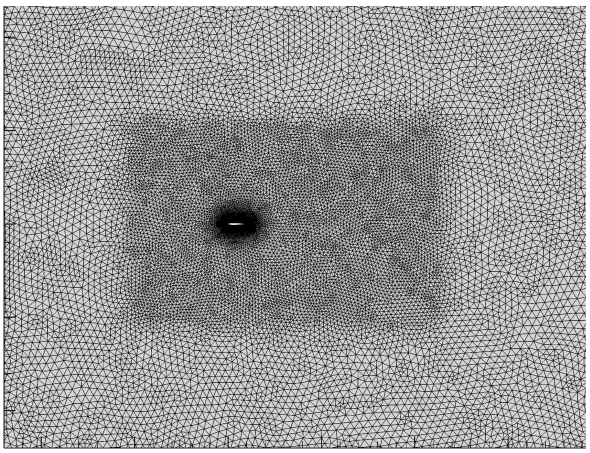

(b) Refinement of the inner domain.

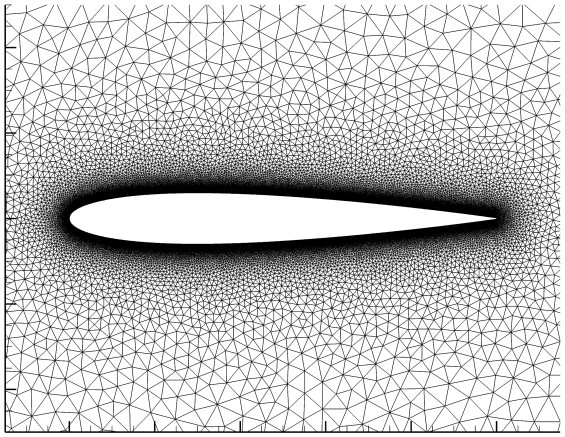

(c) Structured meshes around the profile.

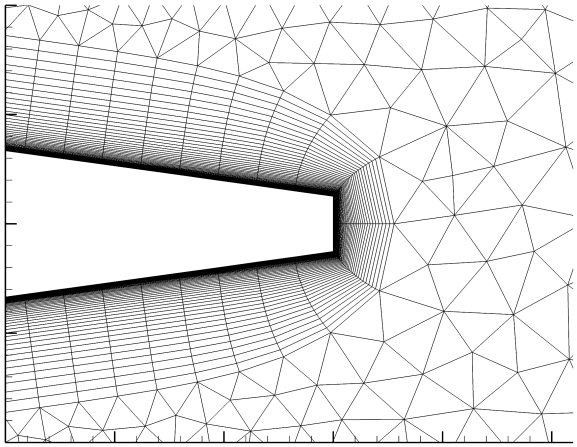

(d) Connection of the structured mesh and the unstructured mesh

Figure 4: Mesh structures and boundary conditions of the test NACA 0012 profile.

model in the near wall region and the $k-\epsilon$ model in the far field. Thus, the $k-\omega$ SST model is applied in this paper for turbulence modelling. The non-dimensional first layer height y^+ is less than 1 for the $k-\omega$ Shear Stress Transport (SST) turbulence model. Based on Re and y^+, the first cell height is 4.46E-6 C_R. The mesh growth rate is 1.1.

3.3. Grid independence

A grid independence test shows that the solutions are independent of the change in grids. This paper refines the mesh based on the chord-wise element size along the rudder profile, which determines the aspect ratio of boundary layers. This parametric refinement addresses the crucial impact factors on the mesh quality and avoids waste of cells by overall refinement (Stern et al., 1999). As the first cell height is 4.46E-6 C_R, the chord-wise element size is tested in range of 2.68×10^{-3} to 2.23×10^{-4}. The corresponding range of aspect ratios is 50 to 600 at an interval of 50. The RANS results are compared to wind-tunnel tests (Ladson, 1988). Fig. 5 presents the relative differences of the lift and drag coefficients with a decrease of the aspect ratio, i.e. an increase of the number of cells, at an angle of attack of 10°. It indicates that the accuracy of the drag coefficient is more sensitive to the number of cells than the accuracy of the lift coefficients. A mesh of 400000 cells can be sufficient to keep the results independent from the grid.

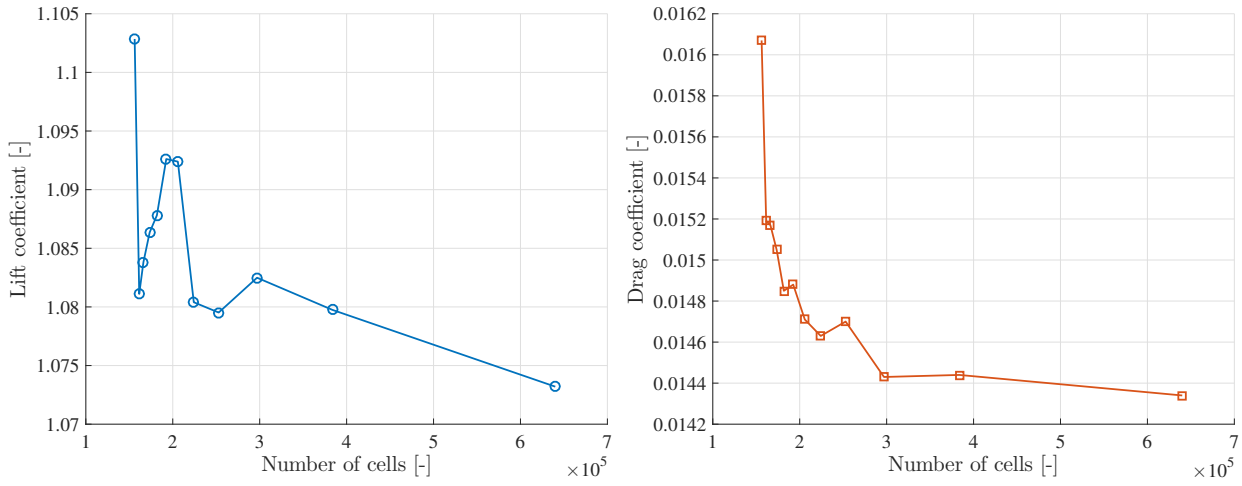

Figure 5: Grid independence study of lift and drag coefficients at an angle of attack of 10°.

3.4. Validation of the RANS method

To validate the RANS method, a classic validation profile NACA 0012 is utilised under angles of attack in a range of 0° to 15° at an interval of 1°. The lift and drag coefficients are compared to one experimental data (Ladson, 1988) and three independent CFD codes (Langley Research Center, 2014), which are CFL3D (NASA LaRC, USA), FUN3D (NASA LaRC, USA), and NTS (NTS, Russia), as shown in Fig. 6. It is worthwhile mentioning that the three

benchmark CFD cases were carried out with structured meshes in a domain of 500 C_R around the profile. Each CFD case has three data points at angles of 5°, 10°, and 15°.

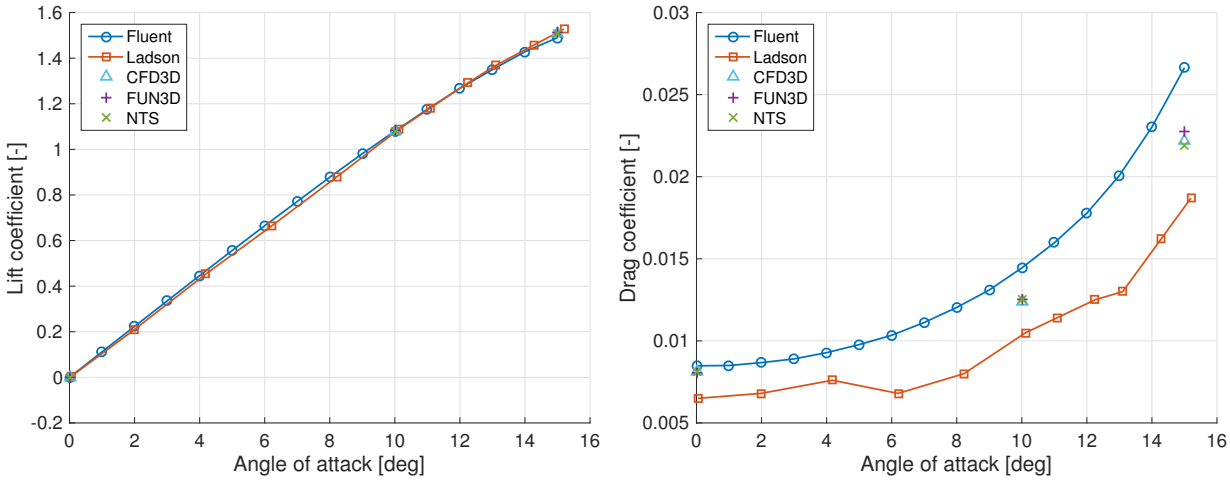

Figure 6: Comparison of Fluent results to numerical and experimental tests.

The comparison in Fig. 6 shows that the RANS method with hybrid meshes predicts the lift coefficient well but overestimates the drag coefficient. Inaccurate lift prediction is mainly due to numerical diffusion. The applied RANS method has a larger overestimation of the drag coefficients than the CFD benchmarks because hybrid meshes introduce larger discretisation errors than the structured meshes applied in the benchmark cases. The overestimation is also partly caused by the assumption that the flow is fully turbulent around the profile while in fact there are always laminar and transition parts near the leading edge (Eleni et al., 2012).

The accuracy of the drag coefficient can be improved by using fully-structured meshes, a larger domain, or more advanced CFD methods like Large Eddy Simulations or Direct Numerical Simulations (DNS). However, these improvements are quite expensive in computation resource and time. Since the drag coefficient is a relatively small value, which contributes to the normal force coefficient much less than the lift coefficient, here we accept the inaccuracy of the drag coefficients for angles in the range of 0° to 15°.

The presented validation proves the usability of the RANS method for the NACA series. For the IFS series, only low-Reynolds-number results were found in the literature, which was given by Thieme (1965). The validation for the IFS series was not performed with these data which may be affected by the low Reynolds number. Since both the NACA and IFS series are well-streamlined profiles, it is reasonable to assume the method is applicable for the IFS series. Yet, no uniform geometry nor validation data for the wedge-tail rudders were available in the literature. The tail shape may cause stronger flow separation than the NACA and IFS series at large angles of attack while not significantly change the stall angle, which causes uncertainty of using the RANS method.

Due to the availability of the experimental data, the validation was only performed for 0° to 15°. For angles of attack larger than 15°, uncertainty is caused by less validation and the strong flow separation, especially for the wedge-tail series. The accuracy of the drag coefficient also becomes more important as its contribution becomes larger to the normal force coefficient. To minimise these uncertainties, in Section 4, the regression formulas of the normal force coefficients are based on the data points in the range of 0° to 10°. The results are shown in the full range of the applied rudder angles, i.e. 0° to 35°, for manoeuvring simulations to show the tendency of the coefficients, but the uncertainty for the results at large angles of attack should be noticed.

4. Hydrodynamic characteristics of various rudder profiles

The RANS method applied in this paper was explained and validated in Section 3. With this RANS method, hydrodynamic characteristics of the rudder profiles, which are introduced in Section 2, are presented in Section 4.1. Accordingly, new regression formulas for rudder normal force coefficients are proposed. Subsequently, the effect of the propeller slipstream (Section 4.2) and the effective aspect ratio (Section 4.3) are considered.

4.1. Rudder hydrodynamic characteristics in 2D open water

2D open-water rudder hydrodynamic coefficients, i.e. the hydrodynamic characteristics of 3D rudders with infinite aspect ratios in open water (C_{N_∞}), are obtained through RANS simulations. Fig. 7 illustrates these results and shows the impact of the profile on rudder efficiency (lift to drag ratios) and effectiveness (normal force coefficients). The NACA series is most efficient while the wedge-tail series is most effective. However, the NACA series and the wedge-tail series are least effective and efficient respectively. It does not seem possible to achieve high efficiency and effectiveness at the same time. The IFS series, which is initially designed for ships (Thieme, 1965), achieves a balance of the efficiency and the effectiveness.

Fig. 7 also shows that thinner NACA profiles have higher lift and drag coefficients than thicker NACA profiles resulting higher normal force coefficients, which are dominated more by the lift coefficients than the drag coefficients. The thickness of the NACA profile does not significantly influence the stall angle. Unlike the NACA series, the thinner wedge-tail and IFS profiles have lower lift coefficients than the thicker ones. In addition, thinner wedge-tail and IFS profiles have higher drag coefficients. Due to the change of the profile thickness (from IFS58 TR15 to IFS61 TR25 and IFS62 TR25), the IFS series has a significant change in the lift coefficient and the stall angle. Moreover, change of the tail thickness (from IFS61 TR25 to IFS62 TR25) extends the stall angle and raises the lift to drag ratio. Compared to the NACA and wedge-tail series, thicker IFS profiles (IFS61 TR25 and IFS62 TR25) have smaller stall angles.

Summarising, various rudder profiles have different hydrodynamic characteristics, which further affect ship manoeuvring performance. The NACA series is most economical. Thus, it is widely applied for ships without critical

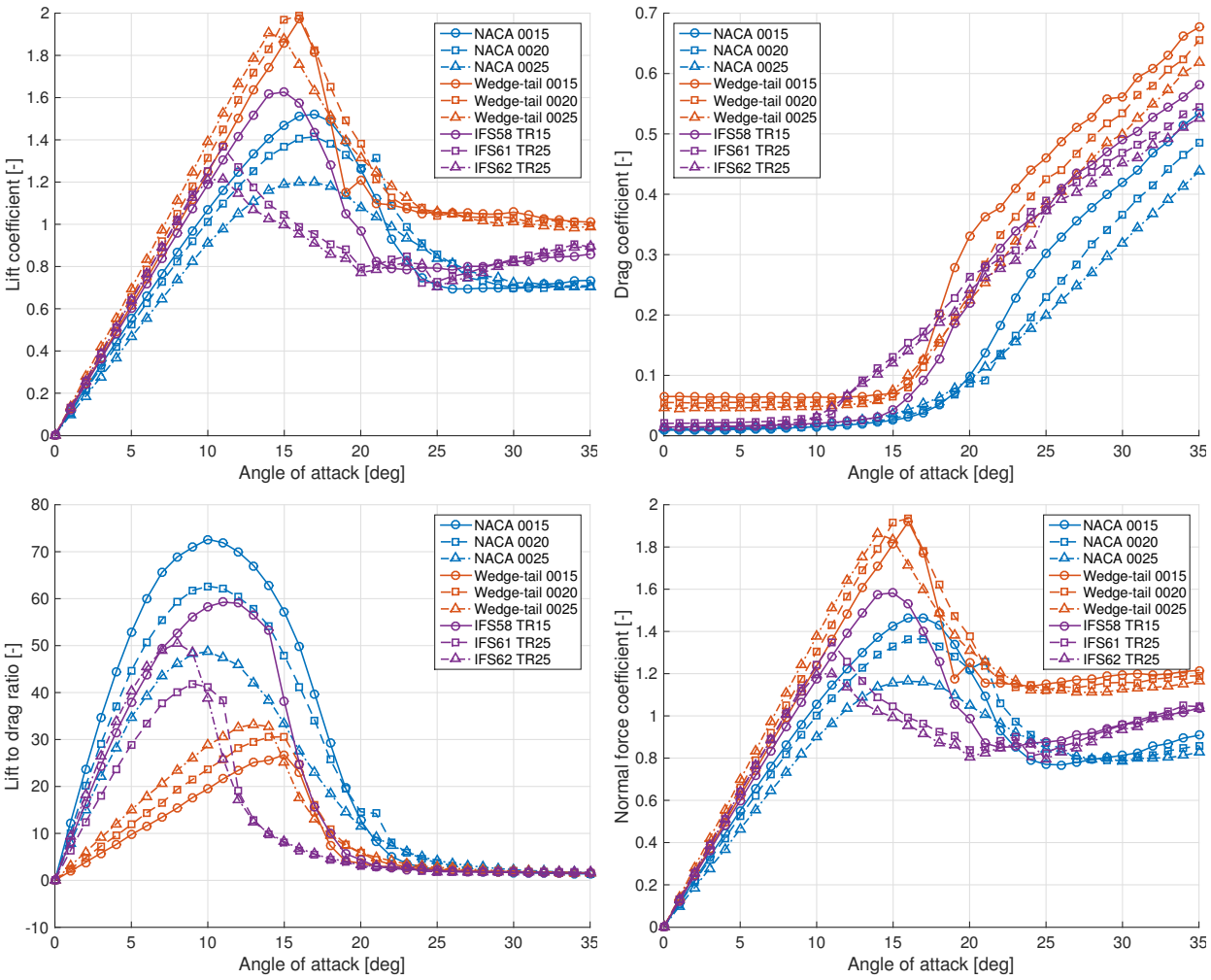

Figure 7: 2D open-water hydrodynamic coefficients of the tested rudder profiles.

manoeuvring requirements. The wedge-tail series is most effective but least efficient. We suggest wedge-tail rudders for ships that need exceptional manoeuvring performance, sail in constrained waterways, or have limited rudder area, for instance, inland vessels. The IFS series can be a good choice when trying to balance efficiency and effectiveness.

4.2. Impact of propeller slipstream on rudder hydrodynamic characteristics

The previous section discussed the rudder hydrodynamics in 2D open water. In reality, ship rudders work in the propeller slipstream. Compared with the rudder working in free stream, Molland and Turnock (1991, 1992) demonstrated a significant increase in the stall angle when the rudder is working behind a rotating propeller. The propeller slipstream may also have impacts on the rudder hydrodynamic coefficients depending on the propeller working load, the propeller revolution, and the arrangement of the propeller and the rudder.

Nienhuis (1987) performed tests for a rudder in open water or in propeller slipstream. The root and tip profiles of the tested rudder are NACA 0018 and NACA 0015 respectively. The chord of the root is 0.130 m and the chord of the tip is 0.095 m. The span of the leading edge is 0.30 m and the span of the trailing edge is 0.28 m. The geometric aspect ratio of the test rudder is 2.58. Nienhuis (1987) tested the rudder at inflow velocity of $1.0\,\mathrm{m\,s^{-1}}$, $1.5\,\mathrm{m\,s^{-1}}$, $2.0\,\mathrm{m\,s^{-1}}$, $2.5\,\mathrm{m\,s^{-1}}$ and $3.0\,\mathrm{m\,s^{-1}}$. However, only the open-water results at $3.0\,\mathrm{m\,s^{-1}}$, i.e. at Re of 3.36×10^5, are compared to results in propeller slipstream to minimise the impact of the Reynolds number.

When the rudder is tested with the propeller, the distance between the propeller hub and the rudder leading edge is 0.115 m. The propeller has a constant revolution per minute (RPM) of 800. The propeller diameter (D_P) is 0.213 m. Three pitch ratios (P_P/D_P) of 0.8, 1.0, and 1.2 are tested at three advance ratios (J_P) of 0.0, 0.2, and 0.4. It is worthwhile to mention that P_P/D_P of the reference KVLCC2 tanker used later in the manoeuvring simulations is 0.721. The tests of the rudder after the rotating propeller refer to a ship advancing with no drift angle. In this paper, the effect of the drift angle is considered in the calculation of the effective rudder angle and rudder inflow velocity. The test results of the rudder alone and the rudder with the propeller from Nienhuis (1987) are adopted and compared in Fig. 8.

As shown in Fig. 8, the propeller slipstream extends the rudder stall angle from the range of 15° to 20° to the range of 30° to 35°. The changes in J_P and P_P/D_P on the lift coefficients are comparatively small to the influence on the drag coefficients. Furthermore, as the drag coefficients are relatively small values compared to the lift coefficients, the impact of these changes are not very significant on the normal force coefficients. According to these results, in this paper, we assume that the effect of the propeller slipstream primarily extends the stall angle without significantly affect the slope of the rudder normal force coefficient. The stall angle is assumed to be extended larger than the maximum effective rudder angle in manoeuvring. Further research is suggested to better represent the impact of the propeller slipstream on rudder hydrodynamics considering the propeller working load and the propeller-rudder arrangements.

Based on our assumption, Table. 1 presents new regression formulas of the normal force coefficients of the rudders

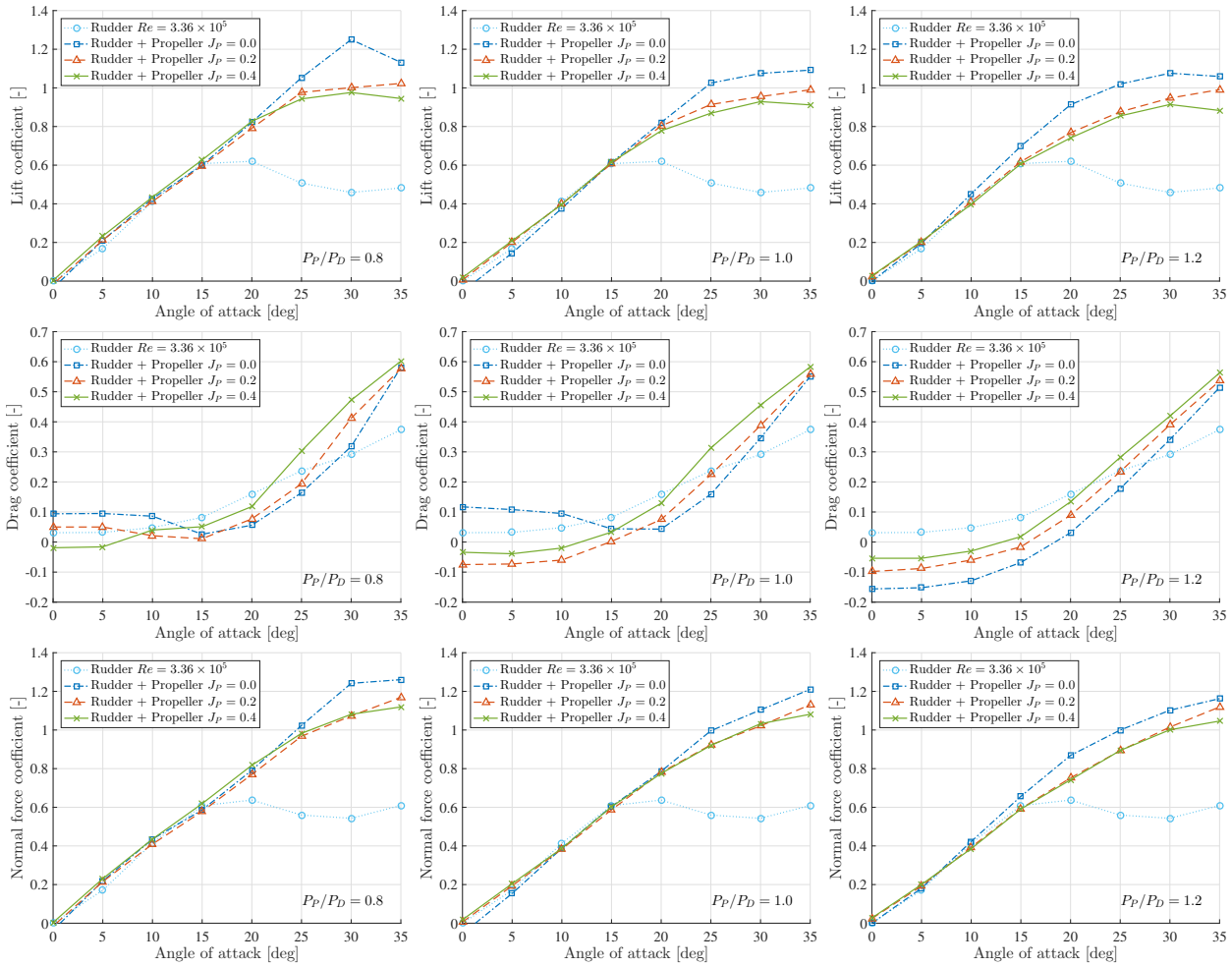

Figure 8: Comparison of the hydrodynamic coefficients of a rudder in open water to those of the rudder in propeller slipstream. Data are adopted from Nienhuis (1987).

with infinite aspect ratio C_{N_∞} for various rudder profiles. These regression formulas are derived from the CFD results given in Fig. 7. The sample points are taken in the range of 0° to 10°. In this range, the accuracy of the RANS results is not significantly affected by the strong flow separation at large angles of attack. We observe that the results of the Fujii formula lie between the RANS predicted NACA 0012 and NACA 0015 profiles.

It should be pointed out that we assume the slope of C_{N_∞} is the same for angles in the range of 0° to 35° and the rudder does not stall in this range. Similar to the original Fujii method, this assumption may overestimate C_{N_∞} at angles in the range of 25° to 35°. For the tested turning and zigzag manoeuvres, the effective rudder angles are either smaller than 25° or larger than 25° for a short time in the whole procedure. Therefore, the error induced by our assumption would be negligible. For manoeuvres that use abnormally large rudder angles, the proposed formulas in Table 1 may not be valid. High-order polynomial or non-linear regressions may improve the usability of the formulas and further research is needed to analyse the uncertainty.

Table 1: Regression formulas of rudder normal force coefficients with an infinite aspect ratio.

Rudder profile	C_{N_∞}
NACA 0012	$6.16 \sin\alpha$
NACA 0018	$5.94 \sin\alpha$
NACA 0015	$6.10 \sin\alpha$
NACA 0020	$5.78 \sin\alpha$
NACA 0025	$5.20 \sin\alpha$
Wedge-tail 0015	$7.12 \sin\alpha$
Wedge-tail 0020	$7.52 \sin\alpha$
Wedge-tail 0025	$7.94 \sin\alpha$
IFS58 TR15	$6.78 \sin\alpha$
IFS61 TR25	$7.19 \sin\alpha$
IFS62 TR25	$7.02 \sin\alpha$
Fujii method (No specific profile)	$6.13 \sin\alpha$

4.3. Impact of the effective aspect ratio on rudder hydrodynamic characteristics

The previous section corrects the 2D open-water rudder normal force coefficients with the propeller slipstream effect. This section considers the rudder aspect ratio effect to transfer the 2D results to 3D. The 2D simulations assume that the rudder has an infinite aspect ratio. Rudders of seagoing ships commonly have aspect ratios in a range of 1.5 to 3.5 while inland vessels typically have rudder aspect ratios around 1.

An increase of the aspect ratio increases the lift slope and reduces the induced drag. Thus, a larger span and aspect ratio is more efficient than a smaller aspect ratio. A large rudder aspect ratio might also achieve a good course-keeping with a high lift curve and rapid response while a small rudder aspect ratio may enhance manoeuvring performance with a large stall angle Molland and Turnock (2007, p. 64). The normal force coefficient with a specific aspect ratio can be estimated based on the normal force coefficient with infinite aspect ratio as the following:

$$C_N = C_{N_\infty} \frac{\Lambda_G}{\Lambda_G + k_\Lambda}, \tag{3}$$

where k_Λ is the rudder aspect ratio impact factor on the normal force coefficient. The existing empirical formula Eq. 2 sets $C_{N_\infty} = 6.13 \sin\alpha$ and $k_\Lambda = 2.25$. In this paper, C_{N_∞} of various rudder profiles are obtained through 2D open-water RANS simulations and corrected with the propeller slipstream effects (Table 1). We take the empirical $k_\Lambda = 2.25$ in terms of the aspect ratio impact factor. A better estimation of k_Λ might be achieved through series of 3D RANS simulations.

5. Manoeuvring modelling

This paper presents manoeuvring simulations of turning and zigzag manoeuvres based on modular models described by Yoshimura and Sakurai (1989); Sano and Yasukawa (2008); Toxopeus (2011); Yasukawa and Yoshimura (2014). The model expresses manoeuvring forces in three categories: the hull, the propeller, and the rudder. Thus, it is capable of analysing the contribution of each component, more specifically the impacts of rudder profiles presented in this paper. Instead of the empirical method for rudder forces, we develop the model based on lift and drag coefficients achieved from RANS simulations. The manoeuvring model is built in MATLAB and named as MatMan. In the following sections, this model produces the results presented under the name of MatMan.

5.1. Coordinate systems

Fig. 9 illustrates the static earth-fixed $o_0 - x_0y_0z_0$ and the dynamic body-fixed $o - xyz$ coordinate systems in this paper. The origin of $o - xyz$ locates on midship o. x, y, and z axes are positive to the bow of the ship, the starboard of the ship, and downwards of the water surface xy respectively. The ship position is determined by the centre of gravity G of the ship in $o_0 - x_0y_0z_0$, which is $(x_G, 0, 0)$ in $o - xyz$ for this three-dimensional model.

If not specified, parameters are defined on midship. Subscript G denotes variables at the centre of gravity. Assuming the ship presented in Fig. 9 is manoeuvring at surge speed u and sway speed v, the ship speed is $V = \sqrt{u^2 + v^2}$. The heading angle ψ, longitudinal speed $u_G = u$, and horizontal speed $v_G = v + x_G r$ express the ship motion state in $o_0 - x_0y_0z_0$. The ship is turning with a rudder angle δ at yaw rate $r = \dot{\psi}$ with a drift angle $\beta = \arctan(-v/u)$.

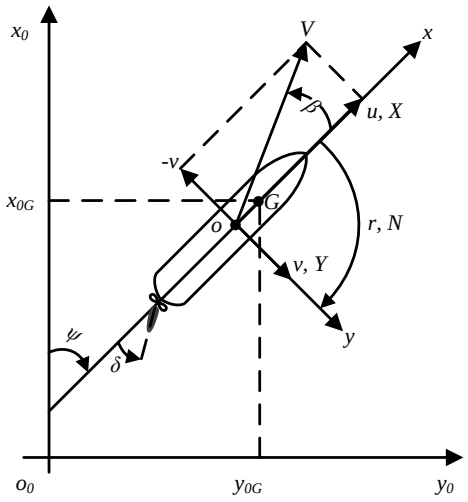

Figure 9: Applied earth-fixed and body-fixed coordinate systems.

The superscript prime denotes the non-dimensional form of velocity u, v, r, forces and moments X, Y, N, mass m, and moments of inertia I_z, J_z, which are non-dimensionalised by ship length between perpendiculars L_{pp}, ship draught T, ship velocity V, and water density ρ as the following:

$$\left.\begin{aligned} u', v' &= \frac{u}{V}, \frac{v}{V} \\ r' &= \frac{rL_{pp}}{V} \\ X', Y' &= \frac{X}{0.5\rho L_{pp} T V^2}, \frac{Y}{0.5\rho L_{pp} T V^2} \\ N' &= \frac{N}{0.5\rho L_{pp}^2 T V^2} \\ I_z', J_z' &= \frac{I_z}{0.5\rho L_{pp}^4 T}, \frac{J_G}{0.5\rho L_{pp}^4 T}. \end{aligned}\right\} \tag{4}$$

5.2. Motion equations

Ship manoeuvring motions in deep clam water are presented with a standard MMG model considering surge, sway, and yaw (Yasukawa and Yoshimura, 2014). This model describes the hydrodynamic force and moment in three aspects: hull, propeller, and rudder. The motion equations are expressed as the following:

$$\left.\begin{aligned} (m + m_x)\dot{u} - (m + m_y)vr - x_G m r^2 &= X_H + X_P + X_R \\ (m + m_y)\dot{v} + (m + m_x)ur + x_G m\dot{r} &= Y_H + Y_R \\ (I_z + x_G^2 m + J_z)\dot{r} + x_G m(\dot{v} + ur) &= N_H + N_R, \end{aligned}\right\} \tag{5}$$

where subscripts H, P, and R denote hull, propeller, and rudder, m is the ship mass, m_x and m_y are added mass due to

motions in surge and sway direction, $\dot{u}$, $\dot{v}$, and $\dot{r}$ are surge, sway, and yaw acceleration, and I_z is the moment of inertia around the centre of gravity, where $I_z \approx (0.25L_{pp})^2 m$.

5.3. Hull force

According to Yasukawa and Yoshimura (2014), hull forces acting on midship X_H, Y_H, and N_H are expressed by polynomials of non-dimensional sway speed v' and yaw rate r' as the following:

$$\left.\begin{aligned} X'_H &= -R'_0 + X'_{vv}v'^2 + X'_{vr}v'r' + X'_{rr}r'^2 + X'_{vvvv}v'^4 \\ Y'_H &= Y'_v v' + Y'_r r' + Y'_{vvv}v'^3 + Y'_{vvr}v'^2 r' + Y'_{vrr}v'r'^2 + Y'_{rrr}r'^3 \\ N'_H &= N'_v v' + N'_r r' + N'_{vvv}v'^3 + N'_{vvr}v'^2 r' + N'_{vrr}v'r'^2 + N'_{rrr}r'^3, \end{aligned}\right\} \tag{6}$$

where R_0 is ship's resistance coefficient in straight moving, X'_{vv}, X'_{vr}, X'_{rr}, X'_{vvvv}, Y'_v, Y'_r, Y'_{vvv}, Y'_{vvr}, Y'_{vrr}, Y'_{rrr}, N'_v, N'_r,N'_{vvv}, N'_{vvr}, N'_{vrr}, and N'_{rrr} are hydrodynamic coefficients on manoeuvring, which are commonly obtained by systematic model tests. The applied hydrodynamic coefficients in this paper were derived by Yasukawa and Yoshimura (2014) through towing tests.

5.4. Propeller force

The hydrodynamic force due to the propeller X_P is expressed by the thrust deduction factor t_P and the propeller thrust T_P as the following:

$$X_P = (1 - t_P)T_P, \tag{7}$$

furthermore, the propeller thrust T_P is written as:

$$T_P = \rho n_P^2 D_P^4 K_T, \tag{8}$$

where n_P is the propeller revolution, D_P is the propeller diameter, and K_T is the propeller thrust coefficient. K_T is commonly expressed by second order polynomials of the propeller advance ratio J_P as:

$$K_T = k_2 J_P^2 + k_1 J_P + k_0, \tag{9}$$

where J_P can be obtained as:

$$J_P = \frac{u(1 - w_P)}{n_P D_P}, \tag{10}$$

where w_P is the wake factor at propeller position in manoeuvring. It is commonly estimated based on the wake factor at propeller position in straight moving w_{P_0} and the geometrical inflow angle to the propeller in manoeuvring β_P. β_P is defined as:

$$\beta_P = \beta - x'_P r', \tag{11}$$

where $x'_P = x_P/L_{pp}$ and x_P is longitudinal potion of propeller. This paper applies the methods of w_P introduced by Yasukawa and Yoshimura (2014) as:

$$(1 - w_P)/(1 - w_{P_0}) = 1 + \{1 - exp(-C_1|\beta_P|)\}(C_2 - 1), \tag{12}$$

where w_{P_0} is the wake factor at propeller position in straight moving, C_1 and C_2 are experimental constants. Furthermore, C_1 and C_2 are different in motions for port and starboard owing to an asymmetric wake factor with respect to the propeller rotational effect.

5.5. Rudder force

Commonly, rudder forces and moments are estimated based on the rudder normal force F_N as the following:

$$\left.\begin{aligned} X_R &= -(1 - t_R)F_N \sin\delta \\ Y_R &= -(1 + a_H)F_N \cos\delta \\ N_R &= -(x_R + a_H x_H)F_N \cos\delta, \end{aligned}\right\} \tag{13}$$

where t_R, a_H, and x_H are hull and rudder interaction parameters, which represents steering resistance deduction factor, rudder force increase factor, and the longitudinal coordinate of the acting point of the additional lateral force respectively, and x_R is the longitudinal position of the rudder. In this article, we assume that these interaction parameters are not influenced by the change of rudder profiles. The rudder tangential force is traditionally neglected as it contributes far less than the rudder normal force to the rudder induced side force for manoeuvring. This assumption is valid for manoeuvres that request rudder angles in a common range of $-35°$ to $35°$. Further study is needed for simulations of manoeuvres with large rudder angles.

F_N is conventionally achieved through Eq. 1 and Eq. 2. When the rudder inflow velocity (V_R) is sufficiently high (the Reynolds number for the rudder is sufficiently high), C_N is independent of the inflow velocity. The propeller slipstream effect on C_N is accounted in Section 4.2. Considering the effect of the effective aspect ratio through Eq. 3, the regression formulas of C_{N_∞} can be transformed to C_N of the rudder with specific aspect ratio in propeller slipstream for manoeuvring simulations. Furthermore, the drift angle at the position of the rudder is considered in the calculation of the effective rudder angle (α_R) as:

$$\alpha_R = \delta - \arctan\frac{v_R}{u_R}. \tag{14}$$

Considering the effect of the propeller on the increment of the rudder inflow velocity, the longitudinal velocity of the inflow to the rudder (u_R) is expressed as:

$$u_R = u(1 - w_R)\sqrt{\eta\left\{1 + \kappa\left[\sqrt{\left(1 + \frac{8K_T}{\pi J^2}\right)} - 1\right]\right\}^2 + (1 - \eta)}, \tag{15}$$

where w_R is the wake factor at the rudder position in manoeuvring, κ is an experimental constant for expressing u_R, and η is the ratio of the propeller diameter to the rudder span. The lateral inflow velocity to the rudder v_R is written as:

$$v_R = V\gamma_R(\beta - \ell'_R r'), \tag{16}$$

where γ_R is the flow straightening factor and different for port and starboard motions, $\ell'_R = \ell_R/L_{pp}$ is the effective longitudinal coordinate of rudder position as described by Yasukawa and Yoshimura (2014).

5.6. Validation of manoeuvring simulation modelling

5.6.1. The reference ship and applied parameters

A KVLCC2 tanker is utilised as the reference ship to validate the manoeuvring model and analyse the impact of rudder profiles on ship manoeuvrability. The KVLCC2 tanker has a single spade-type rudder with a NACA 0018 profile as shown in Fig.1. The free-running model tests carried out by the Maritime Research Institute Netherlands (MARIN) are referred for the validation (Lee et al., 2007; Quadvlieg and Brouwer, 2011). The scale factor is 45.7. Simulations are performed with the same model-scale ship particulars as presented in Table 2. Then, both results of the model-scale simulations and experiments are transformed to full-scale and compared. The applied parameters for simulations are adopted from Yasukawa and Yoshimura (2014) as shown in Table 2.

5.6.2. Validation of turning manoeuvres

The above-mentioned manoeuvring model is applied with the rudder normal force coefficient of a NACA 0018 profile obtained in Section 4. Fig. 11 and Fig. 10 compare the simulated trajectories and histories to the free-running tests of $-35°$ and $35°$ turning manoeuvres (Lee et al., 2007; Quadvlieg and Brouwer, 2011). The simulated turning trajectories roughly agree with the free-running tests. The starboard side turning simulation fits better than the port side simulation. It shows that the manoeuvring model underestimates the asymmetry motions of the port and starboard sides manoeuvres. Table. 3 compares the turning indices of MatMan with the free-running tests (Lee et al., 2007; Quadvlieg and Brouwer, 2011).

Table 2: Applied parameters in the simulations of the KVLCC2 tanker. Source: Yasukawa and Yoshimura (2014).

Main particulars of the KVLCC2 tanker					
L_{pp}	7.0	B_{wl}	1.1688	T	0.455
∇	3.2724	C_b	0.8098	x_G	0.244
m'_x	0.022	m'_y	0.223	J'_z	0.011
u_0	1.179				
Parameters for hull forces and moments					
R'_0	0.022	Y'_v	-0.315	N'_v	-0.137
X'_{vv}	-0.040	Y'_r	0.083	N'_r	-0.049
X'_{vr}	0.002	Y'_{vvv}	-1.607	N'_{vvv}	-0.030
X'_{rr}	0.011	Y'_{vvr}	0.379	N'_{vvr}	-0.294
X'_{vvvv}	0.771	Y'_{vrr}	-0.391	N'_{vrr}	0.0550
		Y'_{rrr}	0.008	N'_{rrr}	-0.013
Parameters for propeller forces and moments					
D_P	0.216	x'_P	-0.48	n_P	10.4
k_0	0.2931	k_1	-0.2753	k_2	-0.1385
t_P	0.220	w_{P_0}	0.40		
Parameters for rudder forces and moments					
A_R	0.0539	Λ_G	1.827	x'_R	-0.50
t_R	0.387	a_H	0.312	x'_H	-0.464
C_1	2.0	C_2 ($\beta_P > 0$)	1.6	C_2 ($\beta_P < 0$)	1.1
γ_R ($\beta_R < 0$)	0.395	γ_R ($\beta_R > 0$)	0.640	ℓ'_R	-0.710
ϵ	1.09	κ	0.50	$\dot{\delta}$	15.8

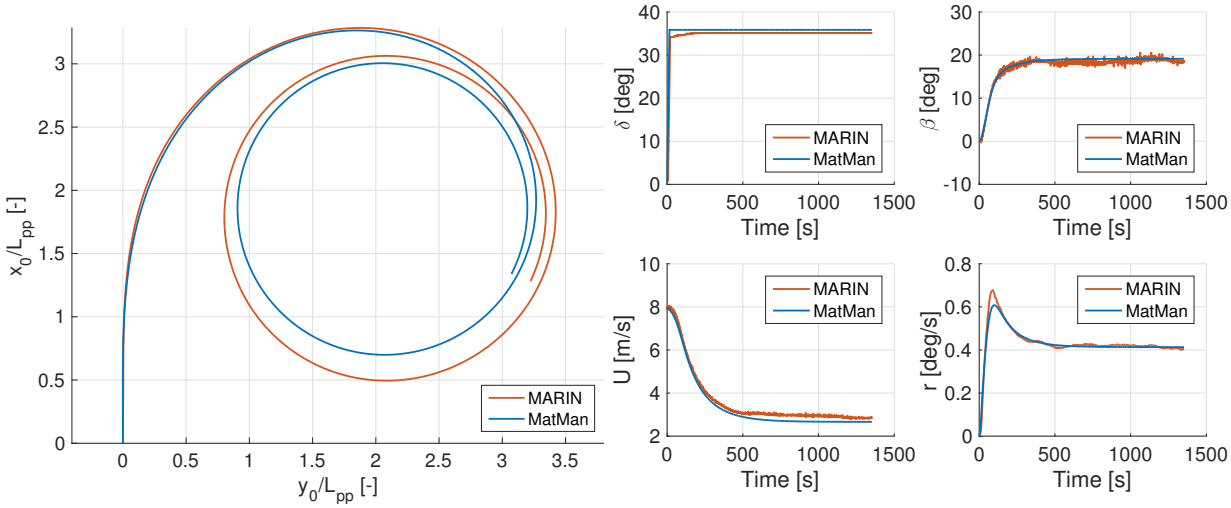

Figure 10: Trajectories and time histories of the simulated and tested motion parameters in the 35° turning manoeuvre.

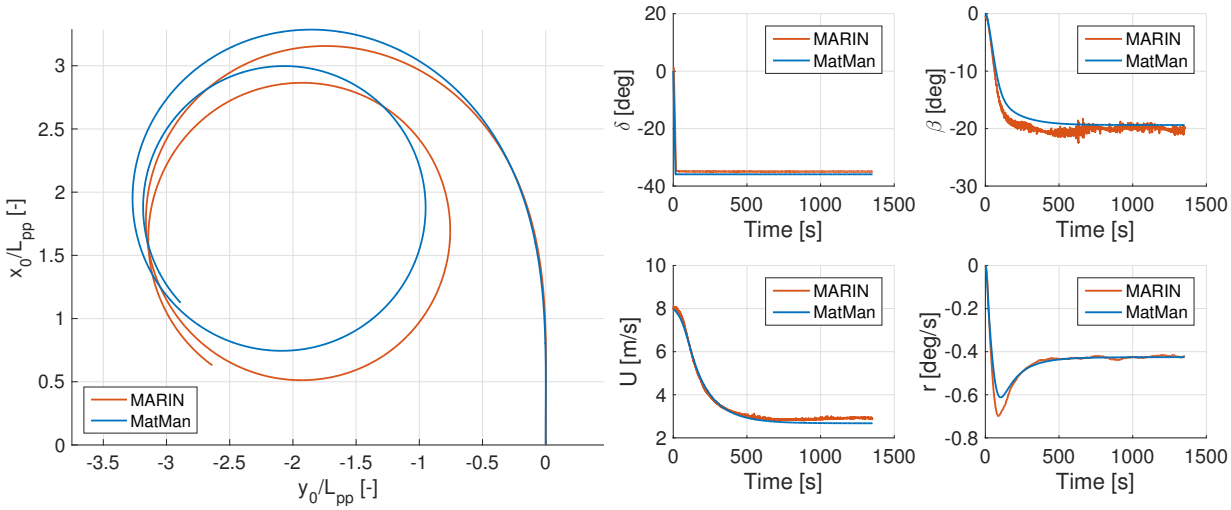

Figure 11: Trajectories and time histories of the simulated and tested motion parameters in the −35° turning manoeuvre.

Table 3: Comparison of the simulated turning indices and the tested turning indices.

Turning criteria	MatMan [−]	MARIN [−]	Relative difference
A'_D ($\delta = 35°$)	3.21	3.07	4.56%
T'_D ($\delta = 35°$)	3.21	3.33	-3.60%
A'_D ($\delta = -35°$)	3.23	2.98	8.39%
T'_D ($\delta = -35°$)	3.21	3.09	3.88%

5.6.3. Validation of zigzag manoeuvres

Fig. 12, Fig. 13, Fig. 14, and Fig. 15 show the trajectories and histories in 10°/10°, −10°/−10°, 20°/20°, and −20°/−20° zigzag manoeuvres respectively. The simulated results roughly agree with the experimental ship motions in zigzag manoeuvres. We observe a larger speed drop in the simulated time histories than the experiments. The histories of rudder angles δ, drift angles β, and turning rates r agree well. Table. 4 compares the simulated overshoot angles to the benchmarks. The manoeuvring indices are underestimated. The largest differences are about 30% in the first and second overshoot angles. It is actually very difficult to predict accurate overshoot angles in degrees. Here, the underestimation is mainly induced by the larger speed decrease, which may be caused by a larger hull damping force calculated in the manoeuvring model.

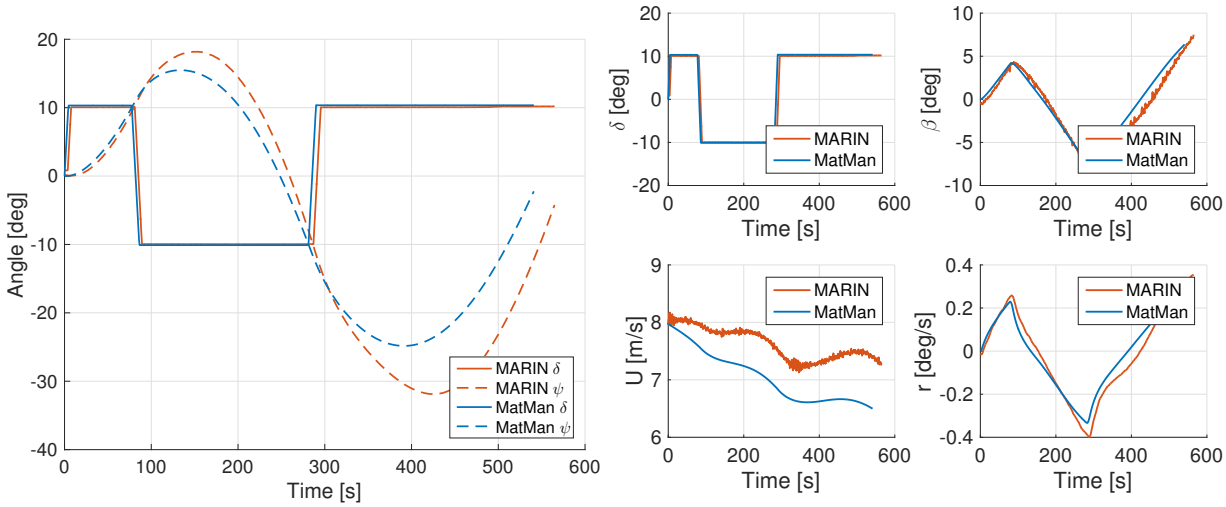

Figure 12: Time histories of the simulated and tested motion parameters in the 10°/10° zigzag manoeuvre.

Table 4: Comparison of the simulated overshoot angles and the tested overshoot angles.

Zigzag criteria	MatMan [°]	MARIN [°]	Relative difference
1st OSA (10°/10°)	5.48	7.9	-30.63%
2nd OSA (10°/10°)	15.14	21.6	-29.91%
1st OSA (20°/20°)	11.11	13.3	-16.47%
1st OSA (−10°/−10°)	7.94	9.3	-14.62%
2nd OSA (−10°/−10°)	9.55	14.7	-35.03%
1st OSA (−20°/−20°)	15.08	14.7	2.59%

Thus far, the applied manoeuvring model, which is a combination of the standard MMG model (Yasukawa and

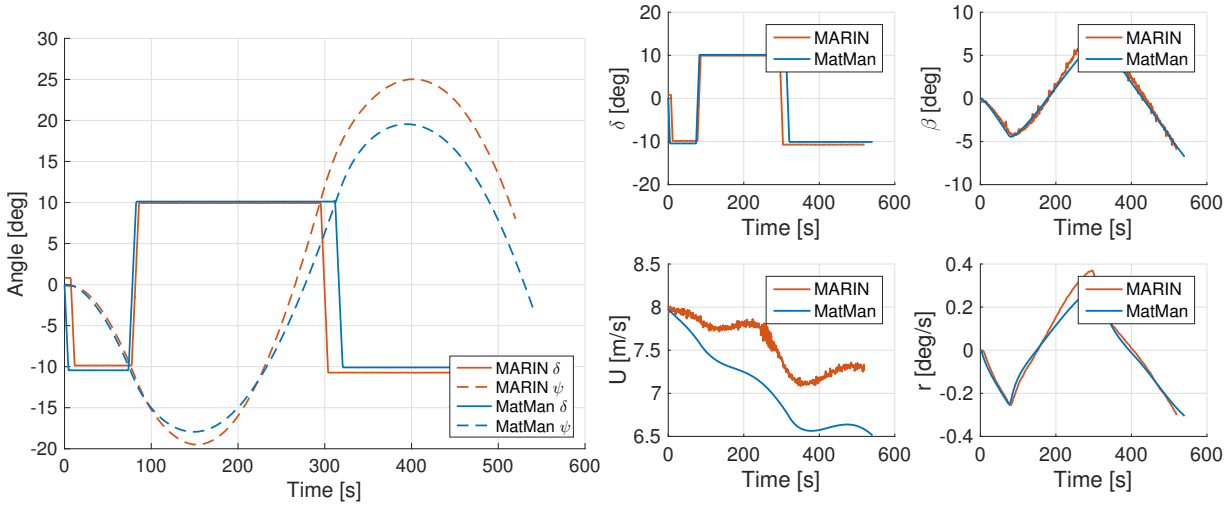

Figure 13: Time histories of the simulated and tested motion parameters in the $-10°/-10°$ zigzag manoeuvre.

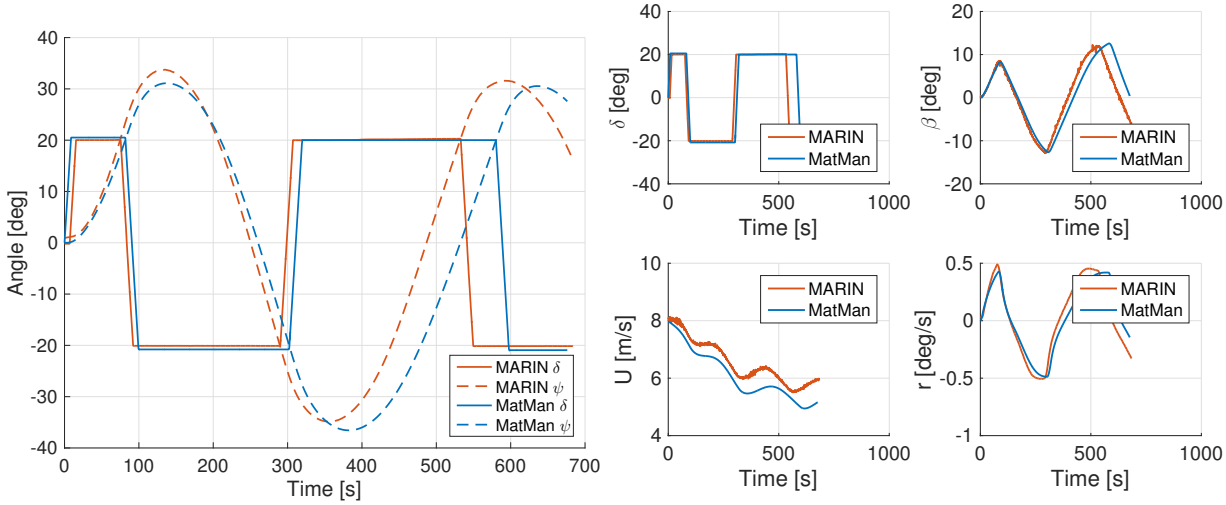

Figure 14: Time histories of the simulated and tested motion parameters in the $20°/20°$ zigzag manoeuvre.

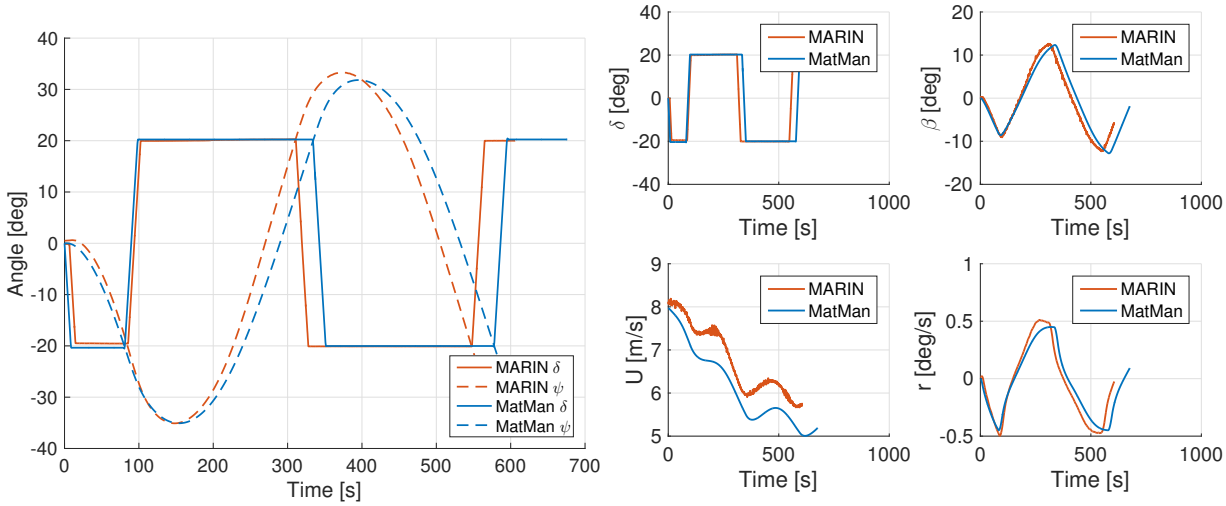

Figure 15: Time histories of the simulated and tested motion parameters in the $-20°/-20°$ zigzag manoeuvre.

Yoshimura, 2014) and RANS-based rudder normal force coefficients, is validated with free-running tests. The model can capture the manoeuvring motions and related parameters. We observe underestimations of the asymmetry motions in turning manoeuvres. Besides the first overshoot angle of $-20°/-20°$ zigzag test, the overshoot angles are underestimated due to a larger speed decrease simulated in the manoeuvring model than experiments. Since the rudder forces and moments are calculated based on a specific profile, the model is applicable to investigate the impacts of rudder profiles on manoeuvring performance.

6. Impacts of rudder profiles on ship manoeuvring

Using the manoeuvring model introduced and validated in the last section, this section presents the manoeuvring performance of the KVLCC2 tanker with various rudder profiles in turning and zigzag manoeuvres.

6.1. Turning manoeuvres

Fig. 16 and Fig. 17 show trajectories of the reference ship with various rudder profiles in $35°$ and $-35°$ turning manoeuvres. As discussed in Section 7, the wedge-tail series can induce larger normal force than the IFS series and the NACA series. Thus, we observe smaller of non-dimensional advances A'_D and tactical diameters T'_D of the trajectories with the wedge-tail profiles than other profiles in Table. 5. Each rudder profile can satisfy the IMO requirements (International Maritime Organization, 2002b,a). The wedge-tail 0025 profile has the smallest turning indices while the NACA 0015 profile gets the largest ones. Thus, we propose the wedge-tail series for ships which require small turning indices,

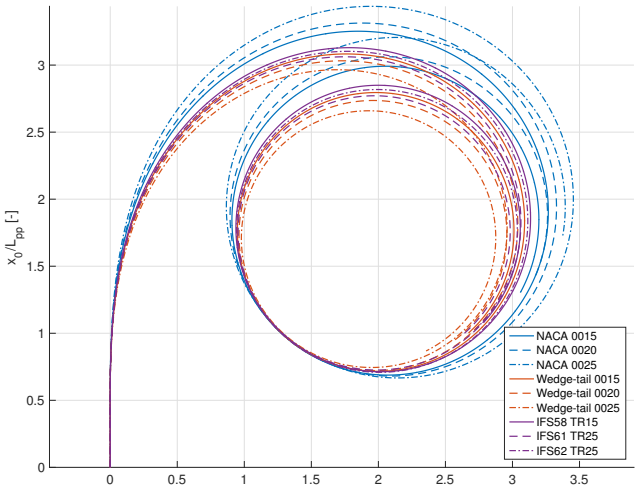

Figure 16: Simulated ship trajectories of 35° turning tests.

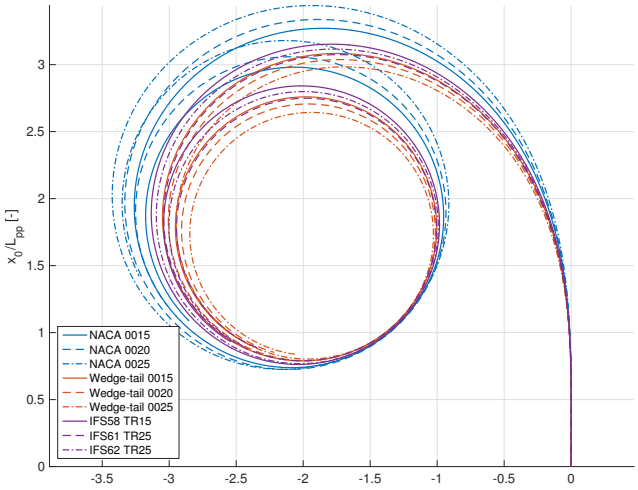

Figure 17: Simulated ship trajectories of −35° turning tests.

Table 5: Comparison of turning indices of the reference ship with various rudder profiles.

Turning criteria	NACA 0015 [−]	NACA 0020 [−]	NACA 0025 [−]
A'_D ($\delta = 35°$)	3.19	3.25	3.38
T'_D ($\delta = 35°$)	3.21	3.27	3.40
A'_D ($\delta = -35°$)	3.21	3.28	3.38
T'_D ($\delta = -35°$)	3.20	3.28	3.37
Turning criteria	Wedge-tail 0015 [−]	Wedge-tail 0020 [−]	Wedge-tail 0025 [−]
A'_D ($\delta = 35°$)	3.02	2.97	2.90
T'_D ($\delta = 35°$)	3.03	2.98	2.90
A'_D ($\delta = -35°$)	3.02	2.98	2.92
T'_D ($\delta = -35°$)	2.99	2.95	2.89
Turning criteria	IFS58 TR15 [−]	IFS61 TR25 [−]	IFS62 TR25 [−]
A'_D ($\delta = 35°$)	3.07	3.00	3.04
T'_D ($\delta = 35°$)	3.08	3.01	3.06
A'_D ($\delta = -35°$)	3.09	3.02	3.06
T'_D ($\delta = -35°$)	3.08	2.98	3.04

6.2. *Zigzag manoeuvres*

Fig. 18, Fig. 19, Fig. 20, and Fig. 21 compare the time histories of rudder angles and heading angles in 10°/10°, −10°/−10°, 20°/20°, and −20°/−20° zigzag tests respectively. Table. 6 presents the overshoot angles of the reference ship with various rudder profiles. The results show that the ship with the wedge-tail series responds faster than the ship with the IFS series or the NACA series, which leads to a smaller period. KVLCC2 with wedge-tail and IFS profile rudders have smaller overshoot angles than ships with NACA profiles. Also the period is decreased significantly.

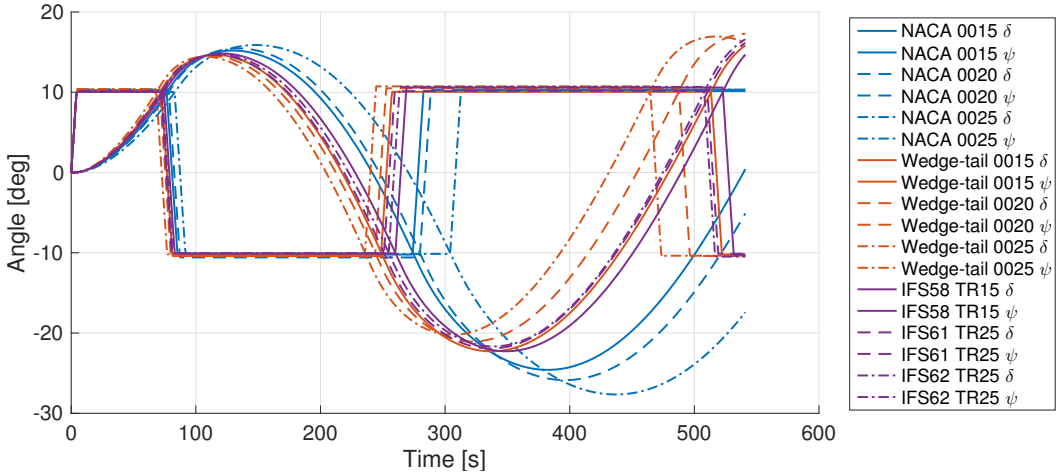

Figure 18: Simulated time histories of rudder angles and heading angles in 10°/10° zigzag tests.

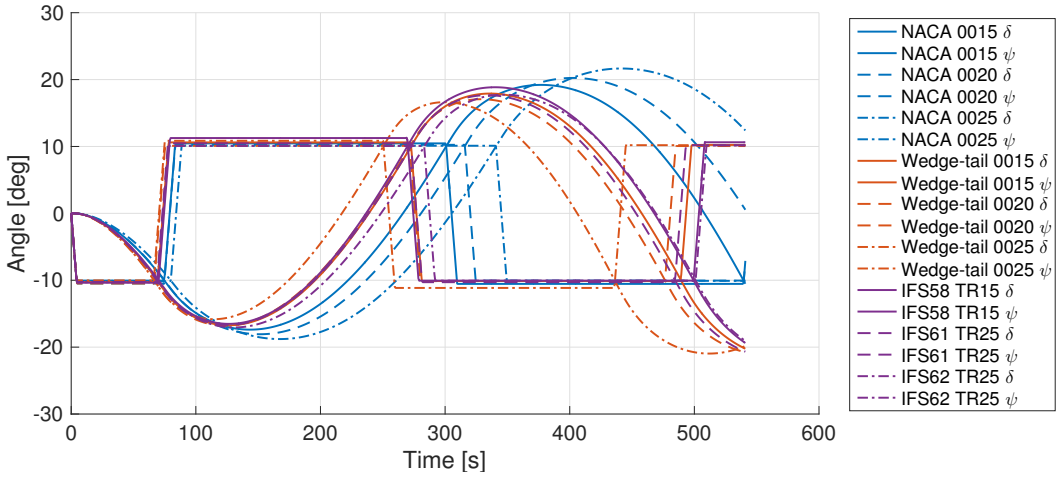

Figure 19: Simulated time histories of rudder angles and heading angles in −10°/−10° zigzag tests.

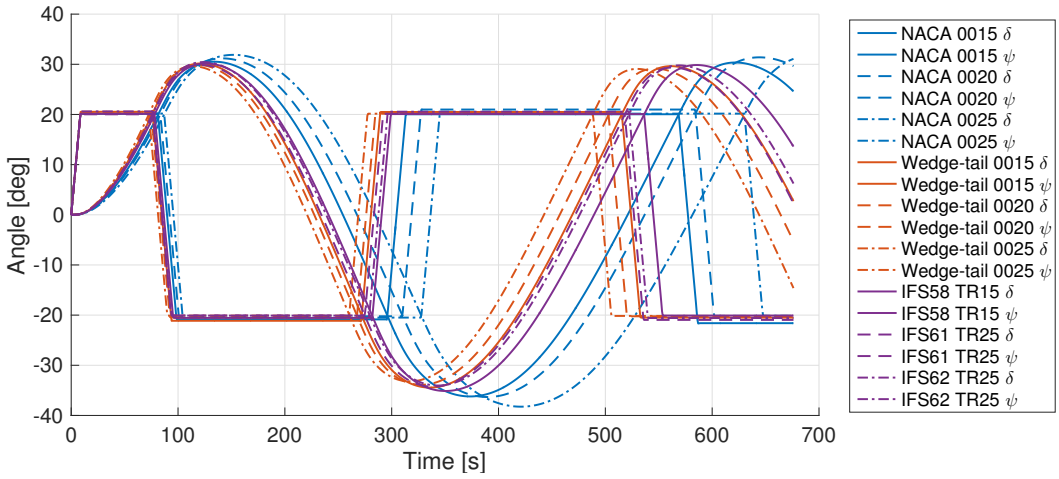

Figure 20: Simulated time histories of rudder angles and heading angles in 20°/20° zigzag tests.

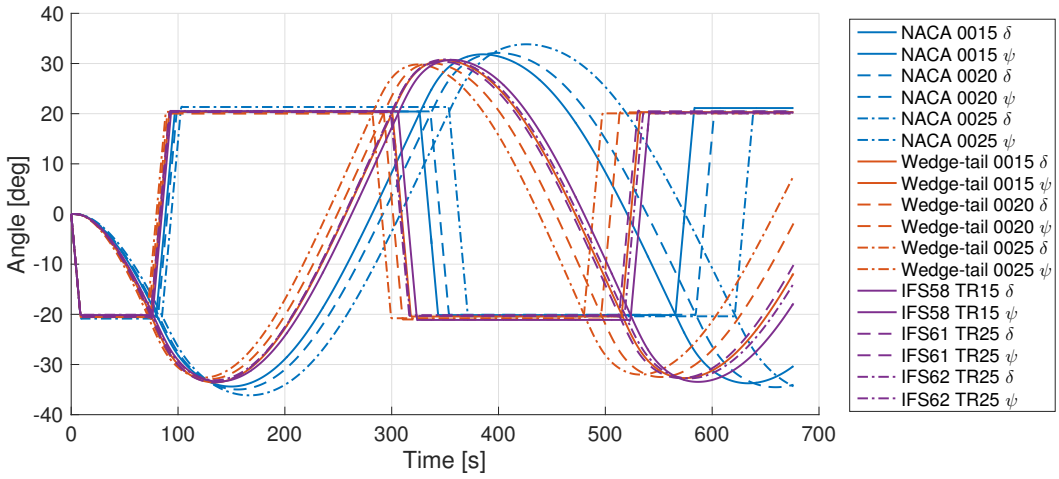

Figure 21: Simulated time histories of rudder angles and heading angles in −20°/−20° zigzag tests.

Table 6: Comparison of overshoot angles of the reference ship with various rudder profiles.

Zigzag criteria	NACA 0015 [°]	NACA 0020 [°]	NACA 0025 [°]
1st OSA (10°/10°)	5.19	5.47	5.88
2nd OSA (10°/10°)	14.58	15.86	17.65
1st OSA (20°/20°)	10.51	11.38	11.88
1st OSA (−10°/−10°)	7.39	8.07	8.79
2nd OSA (−10°/−10°)	9.21	10.25	11.66
1st OSA (−20°/−20°)	14.39	14.98	16.15
Zigzag criteria	Wedge-tail 0015 [°]	Wedge-tail 0020 [°]	Wedge-tail 0025 [°]
1st OSA (10°/10°)	4.66	4.52	4.44
2nd OSA (10°/10°)	12.36	11.51	10.25
1st OSA (20°/20°)	10.17	9.89	9.61
1st OSA (−10°/−10°)	6.73	6.78	5.83
2nd OSA (−10°/−10°)	7.91	7.07	6.63
1st OSA (−20°/−20°)	13.56	12.91	12.61
Zigzag criteria	IFS58 TR15 [°]	IFS61 TR25 [°]	IFS62 TR25 [°]
1st OSA (10°/10°)	4.82	4.66	4.72
2nd OSA (10°/10°)	12.27	11.93	12.27
1st OSA (20°/20°)	10.70	9.85	10.44
1st OSA (−10°/−10°)	6.52	6.68	7.05
2nd OSA (−10°/−10°)	8.85	7.67	7.74
1st OSA (−20°/−20°)	13.39	13.55	13.13

7. Conclusions

In this article, the impacts of rudder profiles were analysed through simulations of turning and zigzag manoeuvres. 2D RANS simulations were first carried out for a range of rudder profiles (NACA series, IFS series, and IFS series) to obtain the rudder hydrodynamic coefficients in open water. Afterwards, the effect of the propeller slipstream and the effective aspect ratio are considered to transfer these 2D results, which can also be considered as 3D results for rudders with infinite geometric aspect ratios, to 3D normal force coefficients with specified geometric aspect ratio. New regression formula of the normal force coefficient was proposed for each rudder profile. Based on a standard MMG manoeuvring model, simulations were done with the proposed formulas assuming a benchmark tanker KVLCC2 with various rudder profiles. The results were summarised achieving the following conclusions:

- Various rudder profiles have different hydrodynamic characteristics, which eventually affect the ship manoeuvrability.
- Among the tested profiles, the wedge-tail series is most effective and the NACA series is most efficient. The IFS series achieves a balance between the efficiency and effectiveness.
- For turning and zigzag manoeuvres, profiles with higher normal force coefficients will result in smaller turning circle test advances and tactical diameters. The overshoot angles in 10/10 and 20/20 zigzag test will reduce.

Ship rudder design primarily depends on the sailing conditions and the ship purpose. In this paper, we analyse the impact of the rudder profiles primarily on the ship manoeuvrability, which is one of the important aspects of rudder design. Other aspects should also be considered to choose a proper rudder such as the rudder induced resistance, the rudder torque, the rudder impact on the propeller performance, and the rudder cavitation. Further research is suggested to improve the efficiency of the rudder while maintaining sufficient effectiveness.

We realise that the above conclusions are achieved based on a marginally directional unstable ship. The reference KVLCC2 tanker fulfils the IMO manoeuvring requirements very well, and in that respect, it is not a challenging ship. The impacts of rudder profiles on ship manoeuvrability for a very directional unstable ship or a directional stable ship require further research. Moreover, the rudder tangential force is neglected in the applied manoeuvring model. Since the tangential force mainly depends on the drag, this simplification may affect the manoeuvring predictions of profiles which have large drag coefficients, for instance, the wedge-tail series presented in this paper.

Acknowledgements

The first author Jialun Liu is financed by the China Scholarship Council under Grant 201206950025.

References

El Moctar, O., 2001. Numerical computations of flow forces in ship manoeuvring. Ship Technology Research 48 (3), 98–123.

Eleni, D. C., Athanasios, T. I., Dionissios, M. P., 2012. Evaluation of the turbulence models for the simulation of the flow over a National Advisory Committee for Aeronautics (NACA) 0012 airfoil. Journal of Mechanical Engineering Research 4 (3), 100–111.

Fujii, H., 1960. Experimental researches on rudder performance (1) (in Japanese). Journal of Zosen Kiokai (107), 105–111.

Fujii, H., Tsuda, T., 1961. Experimental researches on rudder performance (2) (in Japanese). Journal of Zosen Kiokai (110), 31–42.

Fujii, H., Tsuda, T., 1962. Experimental researches on rudder performance (3) (in Japanese). Journal of Zosen Kiokai (111), 51–58.

International Maritime Organization, 2002a. Explanatory Notes to the Standards for Ship Manoeuvrability. MSC/Circ.1053 Adopted 16 December 2012.

International Maritime Organization, 2002b. Standards for Ship Manoeuvrability. Resolution MSC.137(76) Adopted on 4 December 2002.

Keating, M., 2011. Accelerating CFD solutions. ANSYS Advantage, 48–49.

Kim, H. J., Kim, S. H., Oh, J. K., Seo, D. W., 2012. A proposal on standard rudder device design procedure by investigation of rudder design process at major Korean shipyards. Journal of Marine Science and Technology (Taiwan) 20 (4), 450–458.

Ladson, C. L., 1988. Effects of Independent Variation of Mach and Reynolds Numbers on the Low-Speed Aerodynamic Characteristics of the NACA 0012 Airfoil Section. Tech. rep., Langley Research Center, Hampton, Viginia, USA.

Langley Research Center, 2014. Turbulence Modeling Resource.
URL http://turbmodels.larc.nasa.gov/naca0012_val.html

Lee, S. W., Toxopeus, S. L., Quadvlieg, F. H. H. A., 2007. Free Sailing Manoeuvring Tests on KVLCC1 and KVLCC2. Tech. rep., Maritime Research Institute Netherlands (MARIN), Wageningen, The Netherlands.

Liu, J., Hekkenberg, R., 2016. Sixty years of research on ship rudders: Effects of design choices on rudder performance. Ships and Offshore Structures, 1–18.

Liu, J., Hekkenberg, R., Rotteveel, E., Hopman, H., Sep. 2015. Literature review on evaluation and prediction methods of inland vessel manoeuvrability. Ocean Engineering 106, 458–471.

Molland, A. F., Turnock, S. R., Mar. 1991. Wind Tunnel Investigation of the Influence of Propeller Loading on Ship Rudder Performance. Tech. Rep. Ship Science Report No. 46, University of Southampton, Southampton, UK.

Molland, A. F., Turnock, S. R., 1992. Further Wind Tunnel Investigation of the Influence of Propeller Loading on Ship Rudder Performance. Tech. rep., University of Southampton, Southampton, UK.

Molland, A. F., Turnock, S. R., 2007. Marine Rudders and Control Surfaces: Principles, Data, Design and Applications, 1st Edition. Elsevier Butterworth-Heinemann, Oxford, UK.

Nienhuis, U., Jul. 1987. Passieve Manoeuvreerhulpmiddelen: Open Water Proeven met Roer (in Dutch). Tech. rep., Maritime Research Institute Netherlands (MARIN), Wageningen, The Netherlands.

Quadvlieg, F. H. H. A., Brouwer, J., 2011. KVLCC2 benchmark data including uncertainty analysis to support manoeuvring predictions. In: 4th International Conference on Computational Methods in Marine Engineering (MARINE 2011). Lisbon, Portugal.

Sano, M., Yasukawa, H., Apr. 2008. Maneuvering motions of KVLCC1 and KVLCC2 using MMG model. In: SIMMAN 2008: Workshop on Verification and Validation of Ship Manoeuvring Simulation Methods. Copenhagen, Denmark, pp. 51–55.

Söding, H., Aug. 1998. Limits of potential theory in rudder flow predictions. In: 22nd Symposium on Naval Hydrodynamics. Washington, DC, USA, pp. 622–637.

Stern, F., Wilson, R. V., Coleman, H. W., Paterson, E. G., Sep. 1999. Verification and Validation of CFD Simulations. Tech. rep., Iowa Institute of Hydraulic Research, Iowa City, USA.

Thieme, H., 1965. Design of Ship Rudders (Zur Formgebung von Shiffsrudern, originally published in German 1962, translated by E. N. Labouvie). Tech. rep., Shipbuilding Institute, University of Hamburg, Washington, DC, USA.

Toxopeus, S., 2011. Practical Application of Viscous-Flow Calculations for the Simulation of Manoeuvring Ships. Phd's thesis, Delft University of Technology.

Vantorre, M., Oct. 2001. Stationary and non-stationary open water rudder tests. In: Kijima, K. (Ed.), Mini Symposium on Prediction of Ship Manoeuvring Performance. Tokyo, Japan, pp. 103–111.

Yasukawa, H., Yoshimura, Y., 2014. Introduction of MMG standard method for ship maneuvering predictions. Journal of Marine Science and Technology 20 (1), 37–52.

Yoshimura, Y., Sakurai, H., Mar. 1989. Mathematical model for the manoeuvring ship motion in shallow water (3rd report): Manoeuvrability of a twin-propeller twin-rudder ship. Journal of the Kansai Society of Naval Architects, Japan 211, 115–126.